

Impacts of the $^{12}\text{C}(\alpha, \gamma)^{16}\text{O}$ reaction rate on ^{56}Ni nucleosynthesis in pair-instability supernovae

Hiroki Kawashimo,^{1,2*} Ryo Sawada,^{1,3} Yudai Suwa^{1,4} Takashi J. Moriya,^{5,6,7} Ataru Tanikawa^{1,8} and Nozomu Tominaga^{5,6,9}

¹Department of Earth Science and Astronomy, Graduate School of Arts and Sciences, The University of Tokyo, Meguro, Tokyo 153-8902, Japan

²RIKEN Nishina Center for Accelerator-based Science, RIKEN, Wako, Saitama 351-0198, Japan

³Institute for Cosmic Ray Research, The University of Tokyo, Kashiwa, Chiba 277-8582, Japan

⁴Center for Gravitational Physics and Quantum Information, Yukawa Institute for Theoretical Physics, Kyoto University, Kyoto 606-8502, Japan

⁵National Astronomical Observatory of Japan, National Institutes of Natural Sciences, Mitaka, Tokyo 181-8588, Japan

⁶Astronomical Science Program, Graduate Institute for Advanced Studies, SOKENDAI, Mitaka, Tokyo 181-8588, Japan

⁷School of Physics and Astronomy, Faculty of Science, Monash University, Clayton, Victoria 3800, Australia

⁸Center for Information Science, Fukui Prefectural University, Eiheiji, Fukui 910-1195, Japan

⁹Department of Physics, Faculty of Science and Engineering, Konan University, Kobe, Hyogo 658-8501, Japan

Accepted XXX. Received YYY; in original form ZZZ

ABSTRACT

Nuclear reactions are key to our understanding of stellar evolution, particularly the $^{12}\text{C}(\alpha, \gamma)^{16}\text{O}$ rate, which is known to significantly influence the lower and upper ends of the black hole (BH) mass distribution due to pair-instability supernovae (PISNe). However, these reaction rates have not been sufficiently determined. We use the MESA stellar evolution code to explore the impact of uncertainty in the $^{12}\text{C}(\alpha, \gamma)^{16}\text{O}$ rate on PISN explosions, focusing on nucleosynthesis and explosion energy by considering the high resolution of the initial mass. Our findings show that the mass of synthesized radioactive nickel (^{56}Ni) and the explosion energy increase with $^{12}\text{C}(\alpha, \gamma)^{16}\text{O}$ rate for the same initial mass, except in the high-mass edge region. With a high (about twice the STARLIB standard value) rate, the maximum amount of nickel produced falls below $70 M_{\odot}$, while with a low rate (about half of the standard value) it increases up to $83.9 M_{\odot}$. These results highlight that carbon "preheating" plays a crucial role in PISNe by determining core concentration when a star initiates expansion. Our results also suggest that the onset of the expansion, which means the end of compression, competes with collapse caused by helium photodisintegration, and the maximum mass that can lead to an explosion depends on the $^{12}\text{C}(\alpha, \gamma)^{16}\text{O}$ reaction rate.

Key words: stars: massive – supernovae: general – stars: evolution – nuclear reactions, nucleosynthesis, abundances

1 INTRODUCTION

Pair Instability Supernovae (PISNe) are the explosive deaths of very massive stars, which have been theoretically predicted (e.g., Barkat et al. 1967; Fryer et al. 2001; Heger et al. 2003) and a good candidate has recently been discovered (Schulze et al. 2024). In very massive stars that form massive helium cores ($M_{\text{He}} \gtrsim 45 M_{\odot}$; Heger & Woosley 2002), the electron-positron creation reactions take place in the core soften the equation of state, and reduce the adiabatic index γ below $4/3$ (Fraley 1968). To be specific, thermal energy is converted into the rest mass of the electron-positron pairs, decreasing the pressure (Rakavy & Shaviv 1967). The instability induced by this pressure reduction causes the core to collapse, leading to explosive oxygen and silicon burning (Rakavy et al. 1967). If the explosive oxygen burning provides enough energy, its thermonuclear energy can reverse the collapse, leading the entire star to explode with no remnant behind it. It is also predicted from stellar evolutionary theory that when massive progenitors become PISNe, we can observe

the luminous transients (10^{44} erg s^{-1} or brighter at peak) for several months (e.g., Heger & Woosley 2002; Scannapieco et al. 2005; Kasen et al. 2011; Dessart et al. 2013).

Since a PISN completely destroys stars and leaves no compact objects behind, it has been thought that there is a pair-instability mass gap in the black hole mass distribution at $50\text{--}130 M_{\odot}$, corresponding to the progenitors of the mass region where PISN occurs (Heger & Woosley 2002; Woosley et al. 2007; Belczynski et al. 2016; Woosley 2017, 2019; Spera & Mapelli 2017). Hence, the upper limit of the mass gap is considered to be determined by the mass range of PISNe and the lower limit by the transition between PISNe and pulsational pair-instability supernovae (PPISN) (cf. Farmer et al. 2020). However, this conjecture is now challenged by GW190521 which has two black holes with masses of $66^{+17}_{-18} M_{\odot}$ and $85^{+21}_{-14} M_{\odot}$ (Abbott et al. 2020a,b; Estellés et al. 2022), and the PISN condition is required to be reconsidered (cf. Nitz & Capano 2021; Abbott et al. 2024; Kinugawa et al. 2021; Moreno Méndez et al. 2023).

The $^{12}\text{C}(\alpha, \gamma)^{16}\text{O}$ reaction rate is one of the most influential nuclear reactions in the evolution of stars (Tur et al. 2009, 2010), and this is also true for PISNe (Takahashi 2018). However, the

* E-mail: h-kawashimo@g.ecc.u-tokyo.ac.jp

$^{12}\text{C}(\alpha, \gamma)^{16}\text{O}$ reaction rate is difficult to determine experimentally with the current measurement sensitivity and remains highly uncertain (deBoer et al. 2017). Therefore, it is important to perform astrophysical simulations that take this uncertainty into account (e.g., Weaver & Woosley 1993; Kikuchi et al. 2015; Mehta et al. 2022; Farag et al. 2022).

Recently, the uncertainty in the $^{12}\text{C}(\alpha, \gamma)^{16}\text{O}$ reaction rate was found to affect the range of PI mass gaps (Farmer et al. 2019, 2020; Costa et al. 2021) (cf. Mehta et al. 2022). It suggested that black holes can be generated in mass regions previously thought to be PI mass gaps, and has attracted attention in explaining GW190521¹. From there, when considering stellar mass distribution, it is expected that the $^{12}\text{C}(\alpha, \gamma)^{16}\text{O}$ reaction rate also affects the event rate of PISNe (Tanikawa et al. 2023). Thus, the effect of the $^{12}\text{C}(\alpha, \gamma)^{16}\text{O}$ reaction rate on PISNe is a noteworthy issue from the standpoint of optical observations. However, it is not clear how the uncertainties of the $^{12}\text{C}(\alpha, \gamma)^{16}\text{O}$ reaction rate affect the brightness of individual PISNe.

The amount of radioactive nickel ^{56}Ni that determines the brightness of an SN is important as information is directly related to observations. It will be helpful to predict the detectability of PISNe by upcoming observatories (Moriya et al. 2019; Regós et al. 2020; Moriya et al. 2022a,b; Tanikawa et al. 2023; Aguado et al. 2023). In addition, nickel synthesis is also an important topic from galactic chemical evolution since nickel is eventually turned into iron and supplied to space. In this study, we have used stellar evolution calculations to consider PISNe that occur under various $^{12}\text{C}(\alpha, \gamma)^{16}\text{O}$ rates and calculate the amount of ^{56}Ni produced and the explosion energy.

This paper is structured as follows. In section 2, we explain the investigation methods. In section 3, we show our results and discuss our findings. We conclude the paper in Section 4.

2 MODELS AND METHODS

2.1 Setup

We utilize version 15140 of the stellar evolution code MESA (Paxton et al. 2011, 2013, 2015, 2018, 2019; Jermyn et al. 2023) to simulate the evolutionary process of helium cores. These cores either collapse to form black holes or undergo explosive events known as Pair-Instability Supernovae (PISNe). The input parameter configuration is based on the default model choices outlined by Marchant et al. (2019), specifically referred to as the `ppi` setup within MESA-`r15140`². Note that we determined the success or failure of PISN using the same criteria as in Marchant et al. (2019). We suppose that a PISN succeeds when all parts of the star exceed the escape velocity, and the calculation is terminated at that time. We also determine failure based on the central density exceeding $10^{12} \text{ g cm}^{-3}$ and the maximum infall velocity of the central Fe core exceeding $8 \times 10^8 \text{ cm s}^{-1}$.

In our simulations, we initiate the process by employing a non-rotating model of hydrogen-free helium stars with a metallicity of $Z = 10^{-5}$. Given our specific focus on understanding the ^{56}Ni amount and explosion energy in the PISN explosions and resolving the transition

¹ Note that there are many suggestions to fill the PI mass gaps without changing $^{12}\text{C}(\alpha, \gamma)^{16}\text{O}$ reaction rate (e.g. Rodríguez et al. 2019; Di Carlo et al. 2020; Fishbach & Holz 2020; Umeda et al. 2020; González et al. 2021; De Luca et al. 2021; Cruz-Osorio et al. 2021; Tanikawa et al. 2021; Ziegler & Freese 2021; Rizzuto et al. 2022; Costa et al. 2022; Siegel et al. 2022; Ziegler & Freese 2022; Moreno Méndez et al. 2023; Volpato et al. 2023).

² We note that one alteration from the original `ppi` setup involves omitting inlist switching based on helium depletion to avoid potential failures during the handoff between inlists.

between successful PISN and CC models, we conducted calculations using various initial mass ranges. We initially explored a broad range of initial masses, spanning from 40 to 180 M_{\odot} , with increments of 5 M_{\odot} . Within this range, the occurrence of PISN explosions was confirmed through calculations performed in increments of 1 M_{\odot} . Furthermore, we conducted simulations with finer resolution, using increments of 0.1 M_{\odot} near the upper boundary of the mass range and subsequently employing increments of 0.01 M_{\odot} in the immediate vicinity of the uppermost edge (see Appendix D). Our investigated mass range covers between 70 and 150 M_{\odot} near the region of the PISN BH mass gap, as revealed by previous studies (Marchant et al. 2019).

The evolution of helium stars serves as a valuable laboratory for investigating the evolution of massive stars experiencing pair-instability. This is because a majority of massive stars are believed to have shed their outer hydrogen layers, thereby exposing their helium cores. Furthermore, the properties of these stars in their final phase are strongly influenced by the mass of their helium cores (Woosley 2017; Marchant et al. 2019). It is important to note that progenitors of merging binary black holes also undergo the loss of their hydrogen envelopes as a result of binary interactions unless their metallicity is nearly zero or convective overshoot is ineffective (e.g., Tanikawa et al. 2022).

We utilize the `approx21_plus_co56.net` nuclear reactions network integrated into the MESA framework. This network has been proven to be efficient and accurate in estimating explosion energy and the quantity of synthesized ^{56}Ni during explosive nucleosynthesis (Longland et al. 2010; Sallaska et al. 2013; Iliadis et al. 2015, 2016; Farmer et al. 2019). For nuclear reaction rates, we adopt the default rates provided by MESA in this version, which are based on NACRE (Angulo et al. 1999) and JINA REACLIB (Cyburt et al. 2010). However, there is one exception, namely the $^{12}\text{C}(\alpha, \gamma)^{16}\text{O}$ rate, which is discussed in detail in Section 2.2.

For hydrodynamics, the setup uses the HLLC method, which is useful for modeling shock waves (Toro et al. 1994). The simulation is switched from hydrostatic to dynamical when the stellar global stability index falls below its critical value, 4/3. This index is calculated using the local pressure P and the local density ρ , as represented by the equation below:

$$\langle \Gamma_1 \rangle = \frac{\int_0^M \frac{\Gamma_1 P}{\rho} dm}{\int_0^M \frac{P}{\rho} dm}, \quad (1)$$

where Γ_1 is the local first adiabatic exponent. This corresponds to the time when neutrino cooling is progressing rapidly (cf. Marchant et al. 2019; Farmer et al. 2019).

2.2 The treatment of the $^{12}\text{C}(\alpha, \gamma)^{16}\text{O}$ rate

The treatment of the $^{12}\text{C}(\alpha, \gamma)^{16}\text{O}$ rate is the most important part of this paper, and it is essentially based on the previous studies by Farmer et al. (2019, 2020). We utilize STARLIB reaction rate library, which provides the median nuclear reaction rate, $\langle \sigma_{c.s.v} \rangle_{\text{med}}$, and the associated uncertainty factor, f.u., at temperatures ranging from $T = 10^6$ to 10^{10} K (Sallaska et al. 2013). Following the approach of Longland et al. (2010), we assume that all reaction rates provided by STARLIB follow a log-normal probability distribution. The log-normal distribution is characterized by the position parameter μ and spread parameter σ , respectively.

$$P(x) = \frac{1}{\sqrt{2\pi\sigma^2}x} \exp\left(-\frac{(\ln x - \mu)^2}{2\sigma^2}\right). \quad (2)$$

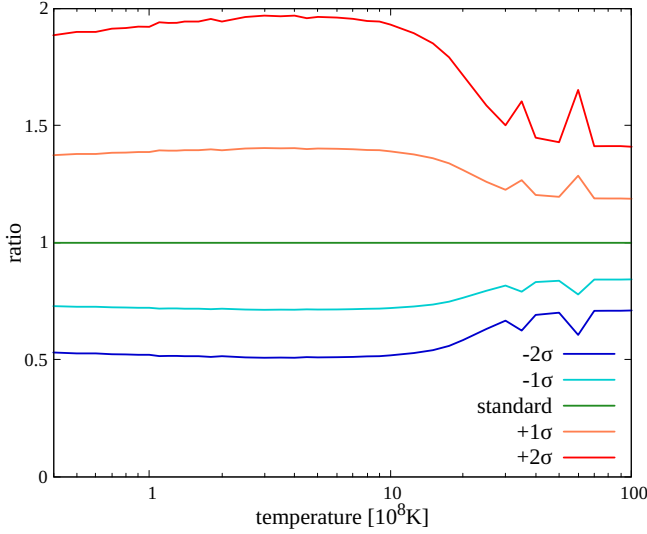


Figure 1. The $^{12}\text{C}(\alpha, \gamma)^{16}\text{O}$ rate as a function of temperature, normalized to the median rate $\langle \sigma_{\text{c.s.v}} \rangle_{\pm n \cdot \sigma} / \langle \sigma_{\text{c.s.v}} \rangle_{\text{med}}$ from STARLIB. $\langle \sigma_{\text{c.s.v}} \rangle_{\text{med}}$ and its uncertainty are from Kunz et al. (2002). The color convention for the $^{12}\text{C}(\alpha, \gamma)^{16}\text{O}$ rate remains consistent throughout our paper.

These parameters can be obtained using the median rate $\langle \sigma_{\text{c.s.v}} \rangle_{\text{med}}$ and the factor uncertainty $f.u.$ represented in STARLIB as follows.

$$\mu = \ln(\langle \sigma_{\text{c.s.v}} \rangle_{\text{med}}), \quad (3)$$

$$\sigma = \ln(f.u.). \quad (4)$$

In a lognormal distribution, the natural logarithm of the random variable ($y = \ln x$) follows a normal distribution. The parameters μ and σ represent the mean and standard deviation of the corresponding normal distribution, respectively. Therefore, in this context, we parameterize the $^{12}\text{C}(\alpha, \gamma)^{16}\text{O}$ reaction in terms of the number of sigmas, $\pm n \cdot \sigma$, from the median STARLIB $^{12}\text{C}(\alpha, \gamma)^{16}\text{O}$ reaction rate:

$$\begin{aligned} \langle \sigma_{\text{c.s.v}} \rangle_{\pm n \cdot \sigma} &\equiv \exp(\mu + n \cdot \sigma) \\ &= \langle \sigma_{\text{c.s.v}} \rangle_{\text{med}} \cdot (f.u.)^{\pm n}. \end{aligned} \quad (5)$$

Figure 1 shows the $^{12}\text{C}(\alpha, \gamma)^{16}\text{O}$ rate as a function of temperature, normalized to the median STARLIB rate $\langle \sigma_{\text{c.s.v}} \rangle_{\pm n \cdot \sigma} / \langle \sigma_{\text{c.s.v}} \rangle_{\text{med}}$. Hereafter, when referring to the reaction rate $\langle \sigma_{\text{c.s.v}} \rangle_{\pm n \cdot \sigma}$, we simply denote it as $\pm n \cdot \sigma$. To examine the effects of $^{12}\text{C}(\alpha, \gamma)^{16}\text{O}$ burning rate, we simulate stellar models using calculated $^{12}\text{C}(\alpha, \gamma)^{16}\text{O}$ rates ranging from -2σ to $+2\sigma$ in increments of 1σ . It is important to note that we refer to the 0σ series — representing the most probable values — as the *standard* series.

3 RESULTS

3.1 Overviews for PISN

In this section, we begin by discussing the typical characteristics of PISNe and the reliability of our explosion model using the standard $^{12}\text{C}(\alpha, \gamma)^{16}\text{O}$ rate. Figure 2 presents the central density and temperature (ρ_c - T_c) trajectories of various stars with different initial He core masses. The $M_{\text{init,He}} = 40 M_{\odot}$ model and the $160 M_{\odot}$

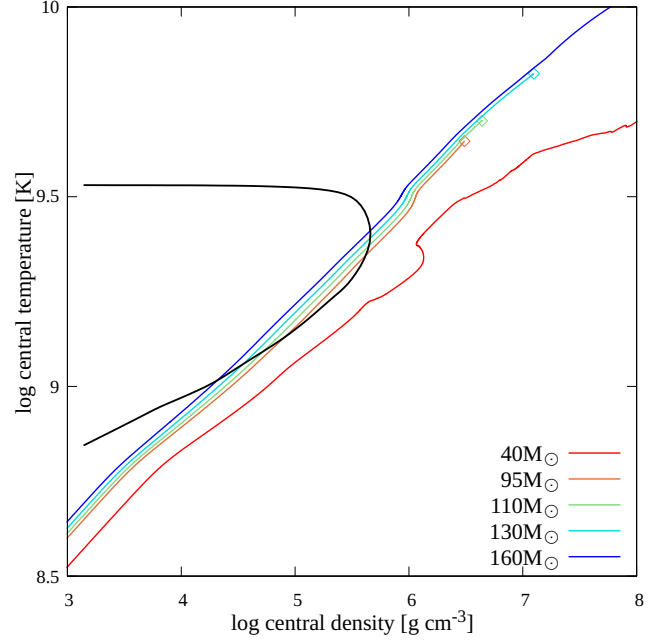


Figure 2. ρ_c - T_c trajectories for models with initial He core masses of 40, 95, 110, 130, and $160 M_{\odot}$, using the standard $^{12}\text{C}(\alpha, \gamma)^{16}\text{O}$ rate. Each color corresponds to the initial mass of the progenitor, except for the black line, which represents $\gamma = 4/3$, the border of gravitational instability. The 40 and $160 M_{\odot}$ models undergo core collapse, while the other models result in PISN explosions. Square points indicate the maximum temperature experienced in exploding models, marking the beginning of the expansion. Beyond these points, the trajectories of explodable models turn back adiabatically.

model both experience iron-core collapse, whereas the other models resulted in PISN explosions. From the figure, it is evident that the ρ_c - T_c of models exceeding $95 M_{\odot}$ enter into the $\gamma < 4/3$ region, whereas the $40 M_{\odot}$ model does not.³

3.2 Effects of the $^{12}\text{C}(\alpha, \gamma)^{16}\text{O}$ reaction rate uncertainty

In Section 3.2, we provide the findings regarding the correlation between the $^{12}\text{C}(\alpha, \gamma)^{16}\text{O}$ rate and the properties of the PISN explosion, specifically the explosion energy, as final total energy (Section 3.2.1) and the synthesis of nickel (Section 3.2.2). Subsequently, we explore the underlying physics behind these correlations in Section 3.2.3. All results are presented in tabular form in Appendix D. We note that the total energy is the sum of kinetic, gravitational, and internal energy. In the final phase, the stars are sufficiently expanded, and no gravitational binding so that the explosion energy is approximately equal to the kinetic energy.

3.2.1 Explosion energy

Figure 3 illustrates the relationship between the explosion energy E_{expl} and the initial He core mass $M_{\text{init,He}}$ for each $^{12}\text{C}(\alpha, \gamma)^{16}\text{O}$ reaction rate. Each color corresponds to a different reaction rate. When we fix the initial He core mass, we observe that models with higher $^{12}\text{C}(\alpha, \gamma)^{16}\text{O}$ rates exhibit higher explosion energies. Furthermore,

³ The global stability of a star is determined by the averaged first adiabatic exponent, see Equation 1.

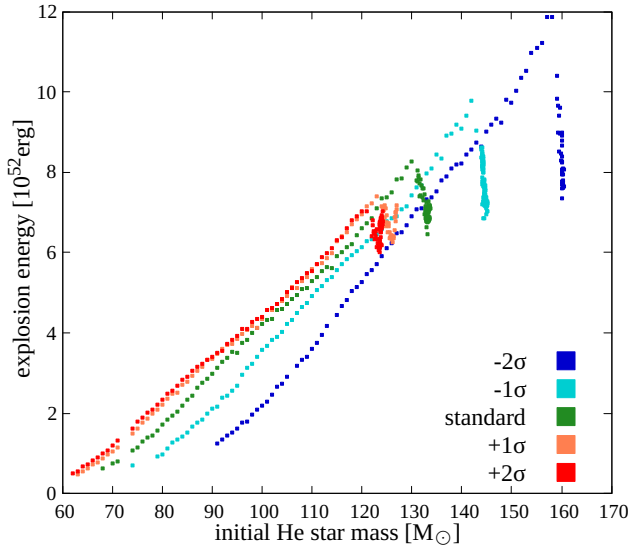


Figure 3. The relationship between the explosion energy E_{exp} and the initial He core mass $M_{\text{init,He}}$ for different $^{12}\text{C}(\alpha, \gamma)^{16}\text{O}$ reaction rates. Each color in the plot corresponds to a specific reaction rate as described in Figure 1.

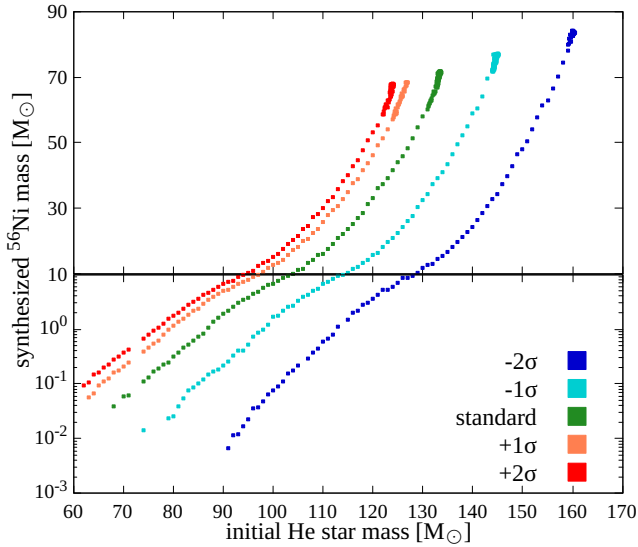


Figure 4. The same plot as Figure 3, but for the synthesized radioactive nickel mass $M_{^{56}\text{Ni}}$ at the final step.

within each series of the same $^{12}\text{C}(\alpha, \gamma)^{16}\text{O}$ rate, we observe a consistent pattern: the explosion energy gradually increases on the low-mass side and then sharply decreases in the high-mass region (for more discussion, see Appendix C). This behavior is observed across all models. In the increasing trend region, we also observe that the maximum explosion energy increases as the $^{12}\text{C}(\alpha, \gamma)^{16}\text{O}$ rate decreases.

3.2.2 ^{56}Ni synthesis

Figure 4 displays the synthesized nickel mass at the final step as a function of the initial helium star mass.⁴ Notably, within the models sharing the same initial mass, a higher $^{12}\text{C}(\alpha, \gamma)^{16}\text{O}$ rate results in increased nickel synthesis. Similar to the explosion energy, we observe that the amount of synthesized nickel in the most massive progenitors is greater at lower $^{12}\text{C}(\alpha, \gamma)^{16}\text{O}$ reaction rates. However, we do not observe a point where the trend abruptly changes within each series.

3.2.3 Carbon "preheating"

Our findings reveal that within the same progenitor mass, a higher $^{12}\text{C}(\alpha, \gamma)^{16}\text{O}$ rate leads to increased total energy and the synthesis of radioactive nickel. This observation aligns with previous studies (Takahashi 2018; Farmer et al. 2020), which suggest that these trends with the $^{12}\text{C}(\alpha, \gamma)^{16}\text{O}$ rate stem from the carbon-burning process preceding the explosive oxygen burning that triggers PISNe.

We describe the "preheating" process by observing energy gaining just before oxygen burning. Figure 5 presents the time trajectories of the total carbon mass and total energy for the initial He core mass $M_{\text{init,He}} = 100M_{\odot}$, in comparison to the standard $^{12}\text{C}(\alpha, \gamma)^{16}\text{O}$ rate and $\pm 2\sigma$ models. The time $t = 0$ corresponds to when the central temperature T_c reaches $\log T_c (\text{K}) = 9.5$ in each model, marking the onset of explosive oxygen burning (Truran & Arnett 1970; Woosley et al. 1973). At high $^{12}\text{C}(\alpha, \gamma)^{16}\text{O}$ reaction rates ($+2\sigma$), the carbon is already depleted at the end of helium burning ($t \approx -80\text{s}$). Consequently, limited carbon burning occurs, and the energy remains stagnant until the onset of explosive oxygen burning. In contrast, at low $^{12}\text{C}(\alpha, \gamma)^{16}\text{O}$ rates, a substantial amount of carbon persists, leading to carbon preheating that boosts the total energy prior to explosive oxygen burning. As a result, the star becomes unbound without awaiting explosive oxygen burning, leading to a gradual growth in total energy. Note that this preheating process is considered to occur within the CO core. This discussion is consistent with the known fact that PISNe are driven by explosive oxygen burning initiated in the CO core.

3.3 The maximum mass limit of the explosion

In this section, we elaborate on the fact that heavier stars become explodable in low $^{12}\text{C}(\alpha, \gamma)^{16}\text{O}$ rate environments. The upper limit of explodable initial mass, which represents the upper boundary of the PI mass gap, is primarily determined by photodisintegration (Takahashi et al. 2016; Takahashi 2018). We anticipate that nickel production and decomposition will transpire concurrently within high-temperature environments. The abundance pattern of a star that undergoes a failed PISN and is just prior to collapse reveals a decrease in nickel around its center, with helium constituting the majority of the components. The two panels in Figure 6 depict the maximum central temperature and the corresponding central density experienced by each model, represented by the square points in Figure 2. Dashed lines in the figure represent the condition for photodisintegration of $^4\text{He} \rightarrow 2n + 2p$, which uses helium produced from $^{56}\text{Ni} \rightarrow 14^4\text{He}$.

⁴ Note that the nickel mass reaches its peak within approximately 100 seconds after the central temperature (T_c) surpasses $10^{9.5}$ K. The amount of nickel remains constant until the completion of the calculation.

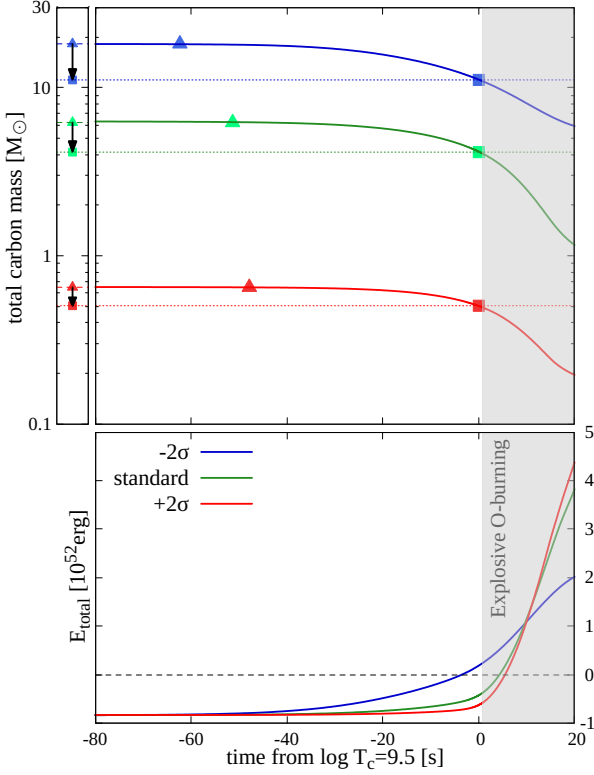


Figure 5. The time evolution of total carbon mass (top panel) and the total energy (bottom panel) for the initial He core mass $M_{\text{He}} = 100M_{\odot}$, comparing the standard and $\pm 2\sigma$ $^{12}\text{C}(\alpha, \gamma)^{16}\text{O}$ rate models. The time origin $t = 0$ is defined as the moment when the central temperature T_c reaches $\log T_c(\text{K}) = 9.5$ in each model, marking the onset of explosive oxygen burning that triggers the PISN. Squares represent the residual carbon mass at $\log T_c(\text{K}) = 9.5$, while triangles correspond to $\log T_c(\text{K}) = 9.3$, which is the beginning of neon burning, it consumes residue of carbon burning. The left panel displays the difference between them. In the bottom panel, the dashed horizontal line indicates the transition between negative and positive total energy.

This condition is given by

$$\log(\rho R(Y_{\text{He}})) = 11.7974 + \frac{3}{2} \log\left(\frac{k_{\text{B}}T}{1\text{MeV}}\right) - 4.097 \left(\frac{k_{\text{B}}T}{1\text{MeV}}\right)^{-1} \quad (6)$$

$$= -3.299 + \frac{3}{2} \log\left(\frac{T}{1\text{K}}\right) - 4.753 \times 10^{10} \left(\frac{T}{1\text{K}}\right)^{-1}, \quad (7)$$

where

$$R(Y_{\text{He}}) = Y_{\text{He}} \left(\frac{1 - Y_{\text{He}}}{Y_{\text{He}}}\right)^{4/3}, \quad (8)$$

and Y_{He} is the residual number fraction of ^4He (see Appendix B for the derivation of Eq. (6) and (7)). Based on Figure 6(a), it is evident that all series of $^{12}\text{C}(\alpha, \gamma)^{16}\text{O}$ rates exhibit nearly identical characteristics. Furthermore, Figure 6(b) demonstrates that the transition from explosion to implosion occurs at $Y_{\text{He}} \approx 0.96$ across all series. This finding suggest that the upper limit of PISNe is determined by the initiation of $^4\text{He} \rightarrow 2\text{n} + 2\text{p}$ photodisintegration.

Figure 7 shows the evolution of central density and temperature for progenitors with $M_{\text{He}} = 115, 120, 125, 130M_{\odot}$. The square points indicate the onset of expansion (see Figure 2), and the trajectories

of the unexploded model are depicted as dashed lines in corresponding colors. This figure also demonstrates that the central evolution of progenitors with the same initial He mass follows a consistent trajectory regardless of the reaction rate. The position of the onset of expansion varies. Moreover, as explained in Figure 2, it is evident that, for a given $^{12}\text{C}(\alpha, \gamma)^{16}\text{O}$ reaction rate, the position of the onset of explosion shifts to higher temperatures and pressures as the mass increases. By combining these results with the discussion in Figure 6, it can be inferred that endpoints associated with higher $^{12}\text{C}(\alpha, \gamma)^{16}\text{O}$ rates surpass the photodisintegration condition at relatively lower masses. Conversely, the endpoints for lower $^{12}\text{C}(\alpha, \gamma)^{16}\text{O}$ reaction rates occur at lower temperatures and pressures, limiting only higher-mass stars to cross the photodisintegration condition. For instance, focusing on the case of $120M_{\odot}$ in Figure 7, higher reaction rates undergo more intense contraction, nearing the He photodisintegration border. When considering $125M_{\odot}$, any progenitors experience higher temperatures and pressures compared to the case of $120M_{\odot}$, resulting in a shift in the endpoint. As a consequence, the $+2\sigma$ model exceeds the He photodisintegration border and fails to explode as PISN. Conversely, the -2σ model, farthest from the He photodisintegration border, remains sufficiently distant even for a $130M_{\odot}$ case, indicating that it would not exceed the He photodisintegration border without becoming even more massive.

4 SUMMARY

We conducted stellar evolution calculations to investigate the impact of $^{12}\text{C}(\alpha, \gamma)^{16}\text{O}$ rates on ^{56}Ni nucleosynthesis in pair-instability supernovae (PISNe). Our findings indicate that lower $^{12}\text{C}(\alpha, \gamma)^{16}\text{O}$ reaction rates result in a greater amount of synthesized nickel in the heaviest explodable progenitor stars. For instance, the upper-mass limit of the synthesized nickel mass changes from $67M_{\odot}$ ($+2\sigma$) to $83M_{\odot}$ (-2σ), corresponding to $125M_{\odot}$ ($+2\sigma$) and $160M_{\odot}$ (-2σ) for the maximum mass of exploding progenitors. The shift of those mass ranges has already found in previous studies for lower-mass side as PPISN-PISN transition line, and our findings are consistent with the same trends for these insights (Regős et al. 2020; Costa et al. 2021; Woosley & Heger 2021). The novelty of this study lies in the systematic calculations of the synthesized nickel mass, which has not been investigated in the previous works. The change in the synthesized nickel mass may be attributed to the carbon preheating process. Additionally, we demonstrated that distinct $^{12}\text{C}(\alpha, \gamma)^{16}\text{O}$ reaction rates give rise to varying ranges of explodable masses due to the interplay between He photodisintegration and the preheating effect.

Note that these results will be affected by the size of the nuclear reaction network. We probably overestimate the amount of nickel produced and the rate of energy absorption by photodisintegration due to the current small network (see Renzo et al. 2020; Farmer et al. 2016, also Appendix C.). However, this overestimation is small enough compared to the amount of change from $^{12}\text{C}(\alpha, \gamma)^{16}\text{O}$ reaction varying. Our main results, therefore, are reliable even after taking into account the uncertainty of the size of the network. On the other hand, it should be noted that some previous studies have shown that larger networks synthesize more nickel (Marchant et al. 2019; Renzo et al. 2020).

Our findings have implications for estimating the detectability of PISNe, particularly regarding their dependence on the $^{12}\text{C}(\alpha, \gamma)^{16}\text{O}$ rate (e.g., Pan et al. 2012; Moriya et al. 2019, 2022a,b; Wong et al. 2019; Regős et al. 2020). Tanikawa et al. (2023) conducted population synthesis calculations to investigate the impact of $^{12}\text{C}(\alpha, \gamma)^{16}\text{O}$ rates on PISN discoveries using the Euclid space tele-

scope (Laureijs et al. 2011). They found that PISNe would be more frequently detected in the standard $^{12}\text{C}(\alpha, \gamma)^{16}\text{O}$ case compared to the -3σ $^{12}\text{C}(\alpha, \gamma)^{16}\text{O}$ case due to a higher intrinsic PISN event rate in the former case. However, their assumptions about identical light curves for PISNe with different $^{12}\text{C}(\alpha, \gamma)^{16}\text{O}$ rates raised concerns about the validity of their results. Finally, our results can address these concerns. Figure 4 indicates that PISNe in the low $^{12}\text{C}(\alpha, \gamma)^{16}\text{O}$ rate case tends to be fainter than those in the standard $^{12}\text{C}(\alpha, \gamma)^{16}\text{O}$ case when the initial He star masses are fixed. Although the maximum luminosity of PISNe gradually increases as $^{12}\text{C}(\alpha, \gamma)^{16}\text{O}$ rates decrease, it will not significantly impact PISN detectability. This is because PISNe with higher He star masses are already rare due to initial stellar mass functions in which the number of stars decreases with their masses increasing (Salpeter 1955; Schneider et al. 2018). In the future, we will further investigate this argument by combining binary population synthesis calculations with PISN light curves, particularly for the low $^{12}\text{C}(\alpha, \gamma)^{16}\text{O}$ case.

ACKNOWLEDGMENTS

H. K. thanks Koh Takahashi, Kanji Mori, Tomoya Takiwaki, and Hiroki Nagakura for fruitful discussions. This work is supported by Grant-in-Aid for Scientific Research (JP18H05437, JP20H00174, JP20H01904, JP21K13966, JP21H04997, JP22KJ0528, JP21K13964, JP22H04571) from the Ministry of Education, Culture, Sports, Science and Technology (MEXT), Japan. HK is supported by RIKEN Junior Research Associate Program.

DATA AVAILABILITY

The data underlying this article will be shared on reasonable request to the corresponding author.

REFERENCES

Abbott R., et al., 2020a, *Phys. Rev. Lett.*, **125**, 101102
 Abbott R., et al., 2020b, *ApJ*, **900**, L13
 Abbott R., et al., 2024, *Phys. Rev. D*, **109**, 022001
 Aguado D. S., et al., 2023, *MNRAS*, **520**, 866
 Angulo C., et al., 1999, *Nuclear Phys. A*, **656**, 3
 Barkat Z., Rakavy G., Sack N., 1967, *Phys. Rev. Lett.*, **18**, 379
 Belczynski K., et al., 2016, *A&A*, **594**, A97
 Costa G., Bressan A., Mapelli M., Marigo P., Iorio G., Spera M., 2021, *MNRAS*, **501**, 4514
 Costa G., Ballone A., Mapelli M., Bressan A., 2022, *MNRAS*, **516**, 1072
 Cruz-Orsorio A., Lora-Clavijo F. D., Herdeiro C., 2021, *J. Cosmology Astropart. Phys.*, **2021**, 032
 Cyburt R. H., et al., 2010, *ApJS*, **189**, 240
 De Luca V., Desjacques V., Franciolini G., Pani P., Riotto A., 2021, *Phys. Rev. Lett.*, **126**, 051101
 Dessart L., Waldman R., Livne E., Hillier D. J., Blondin S., 2013, *MNRAS*, **428**, 3227
 Di Carlo U. N., Mapelli M., Bouffanais Y., Giacobbo N., Santoliquido F., Bressan A., Spera M., Haardt F., 2020, *MNRAS*, **497**, 1043
 Estellés H., et al., 2022, *ApJ*, **924**, 79
 Farag E., Renzo M., Farmer R., Chidester M. T., Timmes F. X., 2022, *ApJ*, **937**, 112
 Farmer R., Fields C. E., Petermann I., Dessart L., Cantiello M., Paxton B., Timmes F. X., 2016, *ApJS*, **227**, 22
 Farmer R., Renzo M., de Mink S. E., Marchant P., Justham S., 2019, *ApJ*, **887**, 53

Farmer R., Renzo M., de Mink S. E., Fishbach M., Justham S., 2020, *ApJ*, **902**, L36
 Fishbach M., Holz D. E., 2020, *ApJ*, **904**, L26
 Fraley G. S., 1968, *Ap&SS*, **2**, 96
 Fryer C. L., Woosley S. E., Heger A., 2001, *ApJ*, **550**, 372
 González E., Kremer K., Chatterjee S., Fragione G., Rodríguez C. L., Weatherford N. C., Ye C. S., Rasio F. A., 2021, *ApJ*, **908**, L29
 Heger A., Woosley S. E., 2002, *ApJ*, **567**, 532
 Heger A., Fryer C. L., Woosley S. E., Langer N., Hartmann D. H., 2003, *ApJ*, **591**, 288
 Iliadis C., Longland R., Coc A., Timmes F. X., Champagne A. E., 2015, *Journal of Physics G Nuclear Physics*, **42**, 034007
 Iliadis C., Anderson K. S., Coc A., Timmes F. X., Starrfield S., 2016, *ApJ*, **831**, 107
 Jermyn A. S., et al., 2023, *ApJS*, **265**, 15
 Kasen D., Woosley S. E., Heger A., 2011, *ApJ*, **734**, 102
 Kikuchi Y., Hashimoto M.-a., Ono M., Fukuda R., 2015, *Progress of Theoretical and Experimental Physics*, **2015**, 063E01
 Kinugawa T., Nakamura T., Nakano H., 2021, *MNRAS*, **501**, L49
 Kunz R., Fey M., Jaeger M., Mayer A., Hammer J. W., Staudt G., Harissopoulos S., Paradellis T., 2002, *ApJ*, **567**, 643
 Laureijs R., et al., 2011, *arXiv e-prints*, p. arXiv:1110.3193
 Longland R., Iliadis C., Champagne A. E., Newton J. R., Ugalde C., Coc A., Fitzgerald R., 2010, *Nuclear Phys. A*, **841**, 1
 Marchant P., Renzo M., Farmer R., Pappas K. M. W., Taam R. E., de Mink S. E., Kalogera V., 2019, *ApJ*, **882**, 36
 Mehta A. K., Buonanno A., Gair J., Miller M. C., Farag E., deBoer R. J., Wiescher M., Timmes F. X., 2022, *ApJ*, **924**, 39
 Moreno Méndez E., De Colle F., López-Cámara D., Vigna-Gómez A., 2023, *MNRAS*, **522**, 1686
 Moriya T. J., Wong K. C., Koyama Y., Tanaka M., Oguri M., Hilbert S., Nomoto K., 2019, *PASJ*, **71**, 59
 Moriya T. J., et al., 2022a, *A&A*, **666**, A157
 Moriya T. J., Quimby R. M., Robertson B. E., 2022b, *ApJ*, **925**, 211
 Nitz A. H., Capano C. D., 2021, *ApJ*, **907**, L9
 Pan T., Kasen D., Loeb A., 2012, *MNRAS*, **422**, 2701
 Paxton B., Bildsten L., Dotter A., Herwig F., Lesaffre P., Timmes F., 2011, *ApJS*, **192**, 3
 Paxton B., et al., 2013, *ApJS*, **208**, 4
 Paxton B., et al., 2015, *ApJS*, **220**, 15
 Paxton B., et al., 2018, *ApJS*, **234**, 34
 Paxton B., et al., 2019, *ApJS*, **243**, 10
 Rakavy G., Shaviv G., 1967, *ApJ*, **148**, 803
 Rakavy G., Shaviv G., Zinamon Z., 1967, *ApJ*, **150**, 131
 Regós E., Vinkó J., Ziegler B. L., 2020, *ApJ*, **894**, 94
 Renzo M., Farmer R., Justham S., Götzberg Y., de Mink S. E., Zapartas E., Marchant P., Smith N., 2020, *A&A*, **640**, A56
 Rizzuto F. P., Naab T., Spurzem R., Arca-Sedda M., Giersz M., Ostriker J. P., Banerjee S., 2022, *MNRAS*, **512**, 884
 Rodríguez C. L., Zevin M., Amaro-Seoane P., Chatterjee S., Kremer K., Rasio F. A., Ye C. S., 2019, *Phys. Rev. D*, **100**, 043027
 Sallaska A. L., Iliadis C., Champagne A. E., Gorieli S., Starrfield S., Timmes F. X., 2013, *ApJS*, **207**, 18
 Salpeter E. E., 1955, *ApJ*, **121**, 161
 Scannapieco E., Madau P., Woosley S., Heger A., Ferrara A., 2005, *ApJ*, **633**, 1031
 Schneider F. R. N., et al., 2018, *Science*, **359**, 69
 Schulze S., et al., 2024, *A&A*, **683**, A223
 Siegel D. M., Agarwal A., Barnes J., Metzger B. D., Renzo M., Villar V. A., 2022, *ApJ*, **941**, 100
 Spera M., Mapelli M., 2017, *MNRAS*, **470**, 4739
 Takahashi K., 2018, *ApJ*, **863**, 153
 Takahashi K., Yoshida T., Umeda H., Sumiyoshi K., Yamada S., 2016, *MNRAS*, **456**, 1320
 Tanikawa A., Kinugawa T., Yoshida T., Hijikawa K., Umeda H., 2021, *MNRAS*, **505**, 2170
 Tanikawa A., Yoshida T., Kinugawa T., Trani A. A., Hosokawa T., Susa H., Omukai K., 2022, *ApJ*, **926**, 83

Tanikawa A., Moriya T. J., Tominaga N., Yoshida N., 2023, *MNRAS*, **519**, L32
 Toro E. F., Spruce M., Speares W., 1994, *Shock Waves*, **4**, 25
 Truran J. W., Arnett W. D., 1970, *ApJ*, **160**, 181
 Tur C., Heger A., Austin S. M., 2009, *ApJ*, **702**, 1068
 Tur C., Heger A., Austin S. M., 2010, *ApJ*, **718**, 357
 Umeda H., Yoshida T., Nagele C., Takahashi K., 2020, *ApJ*, **905**, L21
 Volpato G., Marigo P., Costa G., Bressan A., Trabucchi M., Girardi L., 2023, *ApJ*, **944**, 40
 Weaver T. A., Woosley S. E., 1993, *Phys. Rep.*, **227**, 65
 Wong K. C., Moriya T. J., Oguri M., Hilbert S., Koyama Y., Nomoto K., 2019, *PASJ*, **71**, 60
 Woosley S. E., 2017, *ApJ*, **836**, 244
 Woosley S. E., 2019, *ApJ*, **878**, 49
 Woosley S. E., Heger A., 2021, *ApJ*, **912**, L31
 Woosley S. E., Arnett W. D., Clayton D. D., 1973, *ApJS*, **26**, 231
 Woosley S. E., Blinnikov S., Heger A., 2007, *Nature*, **450**, 390
 Ziegler J., Freese K., 2021, *Phys. Rev. D*, **104**, 043015
 Ziegler J., Freese K., 2022, *arXiv e-prints*, p. arXiv:2212.13903
 deBoer R. J., et al., 2017, *Reviews of Modern Physics*, **89**, 035007

APPENDIX A: ADDITIONAL CONSIDERATIONS ON THE EFFECT OF CARBON PREHEATING ON THE INTERNAL STRUCTURE

We examined the significant impact of carbon preheating prior to oxygen burning on the explosion energy in Section 3.2.3. In this appendix, we present additional findings that shed light on how carbon preheating influences the internal structure of stars. These results offer intriguing insights into the mechanisms through which carbon preheating affects both the explosion energy and the synthesis of nickel.

Figure A1 illustrates the velocity structure of $100M_{\odot}$ progenitors at two different central temperature values: $\log T_c(\text{K}) = 9.2$ (solid lines) and $\log T_c(\text{K}) = 9.45$ (dotted lines). It is important to note that the solid lines correspond to snapshots immediately preceding the triangle points, while the dotted lines correspond to snapshots as just before the square points in Figure 5. Each color represents a different reaction rate (-2σ : blue, standard: green, $+2\sigma$: red). At $\log T_c(\text{K}) = 9.2$ (solid lines), the velocity structure remains relatively consistent across all models, regardless of the reaction rate. The differences in infall speed are at most $\sim 0.2 \times 10^7 \text{ cm s}^{-1}$. However, the preheating effect resulting from carbon combustion leads to noticeable variations in the infall velocity in low $^{12}\text{C}(\alpha, \gamma)^{16}\text{O}$ rate environments, slowing it down by approximately $\sim 5 \times 10^7 \text{ cm s}^{-1}$. Similarly, in high $^{12}\text{C}(\alpha, \gamma)^{16}\text{O}$ rate environments, the infall progresses more rapidly, by $\sim 1 \times 10^7 \text{ cm s}^{-1}$ (although not as fast as in the low (-2σ) and standard cases). Although this specific condition requires more detailed discussion, one possibility is that the enriched "preheating" may be making the star less compact. These findings indicate that carbon preheating contributes to the expansion of the star, rendering it "softer," and provide insights into the differential responses to subsequent explosive oxygen burning.

In fact, the evolution during implosion is influenced by the expansion effect of carbon preheating. Figure A2 shows the time evolution of central temperature and central density in $100M_{\odot}$ progenitors. The dashed lines represent the time at $\log T_c(\text{K}) = 9.3$, marking the onset of carbon preheating. Focusing on these dashed lines, there are differences of ten seconds in the time from the start of preheating until reaching oxygen burning, depending on the reaction rate. Furthermore, it is observed that the lower the reaction rate, the slower the density increases in the preheating region.

These results suggest that stars with a significant amount of remaining carbon are capable of withstanding the dynamical compression with carbon preheating. While the evidence is not yet conclusive, we anticipate that this phenomenon contributes to the differences observed in the synthesized ^{56}Ni mass and explosion energy, as discussed in section 3.

APPENDIX B: THE CALCULATION ABOUT $^4\text{He} \rightarrow 2n+2p$ PHOTODISINTEGRATION

In this appendix, we derive Eq.(6). Note that we use the following notations: "p" represents a proton, "n" represents a neutron, and "He" represents ^4He .

Here, we assume that the nuclear formation and disintegration are in chemical equilibrium, described by the reaction:

$$^4\text{He} \rightleftharpoons 2p + 2n - 28.3\text{MeV}. \quad (\text{B1})$$

Then, the abundances in nuclear equilibrium are given by the Saha's equation,

$$\frac{n_p^2 n_n^2}{n_{\text{He}}} = \frac{g_p^2 g_n^2}{g_{\text{He}}} \left(\frac{2\pi k_B T}{h^2} \right)^{9/2} \left(\frac{m_p^2 m_n^2}{m_{\text{He}}} \right)^{3/2} \exp\left(-\frac{Q}{k_B T}\right), \quad (\text{B2})$$

where n_i is the number density, g_i is the spin degree of freedom, and m_i is the mass for i particle, respectively. The number density is expressed by

$$n_i = \frac{\rho Y_i}{m_i}, \quad (\text{B3})$$

where Y_i is the number fraction and ρ is the density. From reaction (B1), we note that $Q = 28.3\text{MeV}$. Also

$$\frac{g_p^2 g_n^2}{g_{\text{He}}} = 8 \quad (\because g_p = g_n = g_{\text{He}} = 2), \quad (\text{B4})$$

and

$$n_p = n_n. \quad (\text{B5})$$

By assuming

$$m_p \approx m_n \approx \frac{m_{\text{He}}}{4}, \quad (\text{B6})$$

we get

$$n_p + n_n + 4n_{\text{He}} = \frac{\rho}{m_p}. \quad (\text{B7})$$

Combining these equations, we obtain

$$Y_p = \frac{1}{2}(1 - Y_{\text{He}}), \quad (\text{B8})$$

which gives

$$n_p = 2 \frac{1 - Y_{\text{He}}}{Y_{\text{He}}} n_{\text{He}}. \quad (\text{B9})$$

As a result, LHS of Eq. (B2) is rewritten as

$$\frac{n_p^2 n_n^2}{n_{\text{He}}} = 16 \left(\frac{1 - Y_{\text{He}}}{Y_{\text{He}}} \right)^4 n_{\text{He}}^3. \quad (\text{B10})$$

Thus Eq. (B2) reads

$$n_{\text{He}} = 2^{-1/3} \left(\frac{1 - Y_{\text{He}}}{Y_{\text{He}}} \right)^{-4/3} \left(\frac{2\pi k_B T}{h^2} \right)^{3/2} \left(\frac{m_p^2 m_n^2}{m_{\text{He}}} \right)^{1/2} \exp\left(-\frac{Q}{3k_B T}\right). \quad (\text{B11})$$

Substituting constants ($m_p, m_n, m_{\text{He}}, h$ in cgs unit), we get

$$\rho R(Y_{\text{He}}) = 7.9286 \times 10^{11} \left(\frac{k_{\text{B}}T}{1\text{MeV}} \right)^{3/2} \exp\left(-9.433 \frac{1\text{MeV}}{k_{\text{B}}T}\right), \quad (\text{B12})$$

where $R(Y_{\text{He}})$ is presented by Eq. (8).

Finally, taking the logarithm of Eq.(B12), we obtain

$$\log(\rho R(Y_{\text{He}})) = 11.7974 + \frac{3}{2} \log\left(\frac{k_{\text{B}}T}{1\text{MeV}}\right) - 4.097 \frac{1\text{MeV}}{k_{\text{B}}T}, \quad (\text{B13})$$

which is Eq. (6).

APPENDIX C: COMPARISON WITH THE PREVIOUS WORK

In this appendix, we validate the reliability of our calculations by comparing them to previous studies that employed alternative calculation methods.

Figure C1 illustrates the relationship between the initial He core mass $M_{\text{init,He}}$ and (a) the final energy of the explosion E_{expl} , and (b) the synthesized ^{56}Ni mass. These plots represent models with a standard $^{12}\text{C}(\alpha, \gamma)^{16}\text{O}$ rate. We have included the results by Heger & Woosley (2002) for comparison. We confirm a positive correlation between the amount of synthesized ^{56}Ni and the explosion energy for the initial He core mass. Importantly, our results obtained without magnification of the $^{12}\text{C}(\alpha, \gamma)^{16}\text{O}$ rate show reasonable consistency with previous studies.

Note that in Figure C1(a), also in Figure 3, we observe a drop in the explosion energy at the heavier end of the initial He core mass, which has not been reported in previous studies (e.g., Heger & Woosley 2002). It is possible that the explodable upper mass limit of PISNe, primarily governed by He photodisintegration, leads to the "freeze-out" of photodisintegrated elements from iron, resulting in a portion of the explosion energy being captured as rest mass energy. However, it is important to note that this is speculative, and we have not identified the exact physical cause of this trend.

APPENDIX D: DATA TABLE

We present values of the synthesized mass of ^{56}Ni and the explosion energy for all the models that explode as PISN resulting from this study in Table D1 to D5.

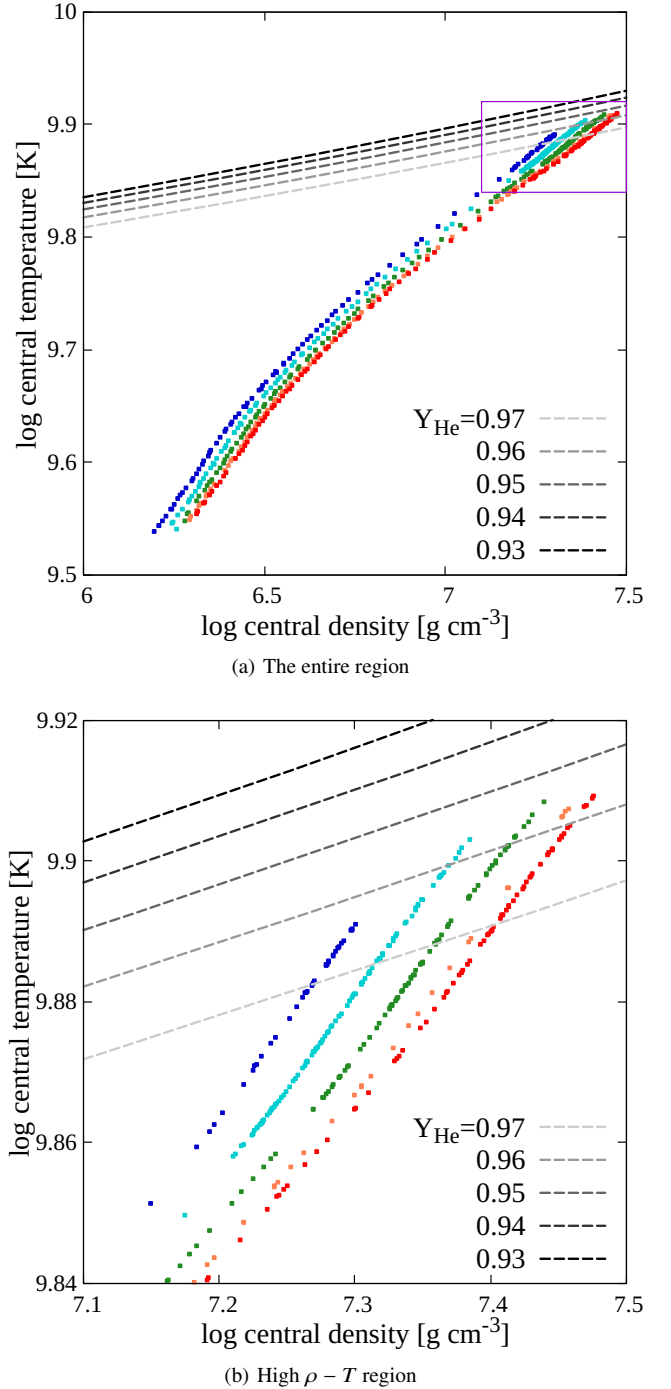


Figure 6. The maximum central temperature and corresponding central density reached by each model. The colors represent different reaction rates, following the same convention as Figure 1. The top panel (a) displays all exploding models, while the bottom panel (b) zooms in on the region highlighted in purple in panel (a). The grey dashed lines indicate the threshold for $^4\text{He} \rightarrow 2n + 2p$ photodisintegration with various Y_{He} .

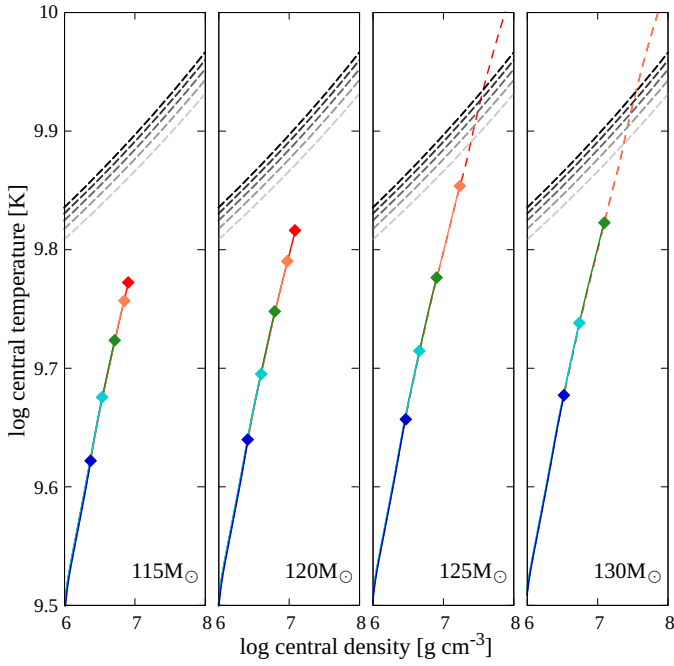


Figure 7. The $\rho_c - T_c$ trajectories for different initial helium core masses: $115M_\odot$ (left panel), $120M_\odot$ (middle left panel), $125M_\odot$ (middle right panel), and $130M_\odot$ (right panel). Each trajectory is assigned a color corresponding to the reaction rate, and the grey dashed lines indicate the threshold for $^4\text{He} \rightarrow 2n + 2p$ photodisintegration (see Figure 6). The square points represent the endpoints, indicating the beginning of the expansion phase, it corresponds with square points in figure 2. The dashed lines represent the trajectories of unexploded models. It is noteworthy that in all panels, the trajectories largely overlap, as the stars undergo similar evolution regardless of the $^{12}\text{C}(\alpha, \gamma)^{16}\text{O}$ rate.

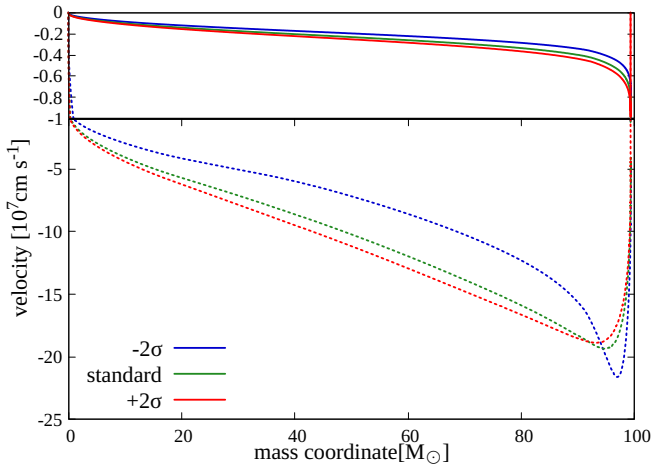


Figure A1. The velocity profiles of different parts of a $100M_\odot$ model. The solid line corresponds to the velocity just before the onset of carbon preheating ($T_c = 9.2$), while the dotted line represents the velocity just before the start of oxygen burning ($T_c = 9.45$).

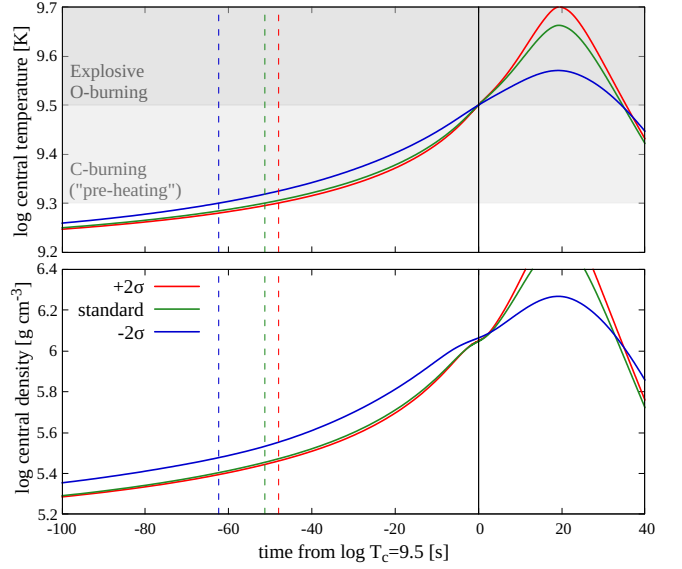


Figure A2. The time evolution of the central temperature (top panel) and central density (bottom panel) for models with an initial helium star mass of $100M_\odot$. The dashed vertical lines represent the instances when $\log T_c(\text{K}) = 9.3$, indicating the initiation of carbon preheating.

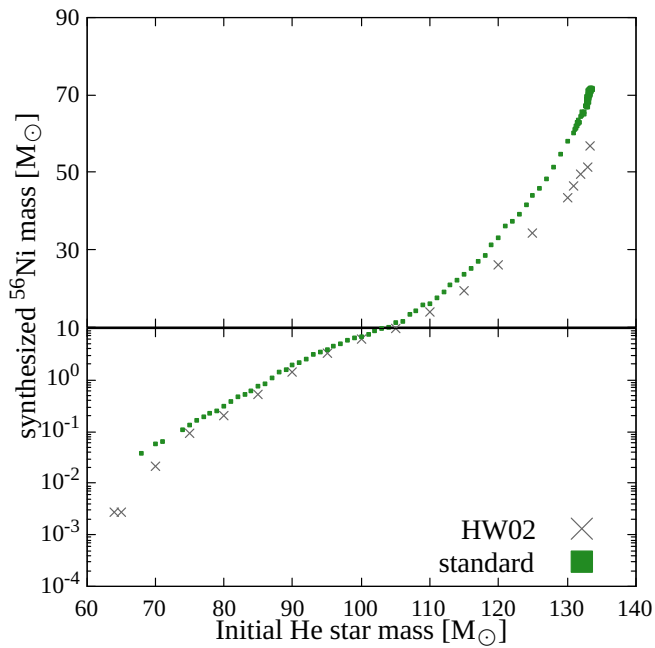
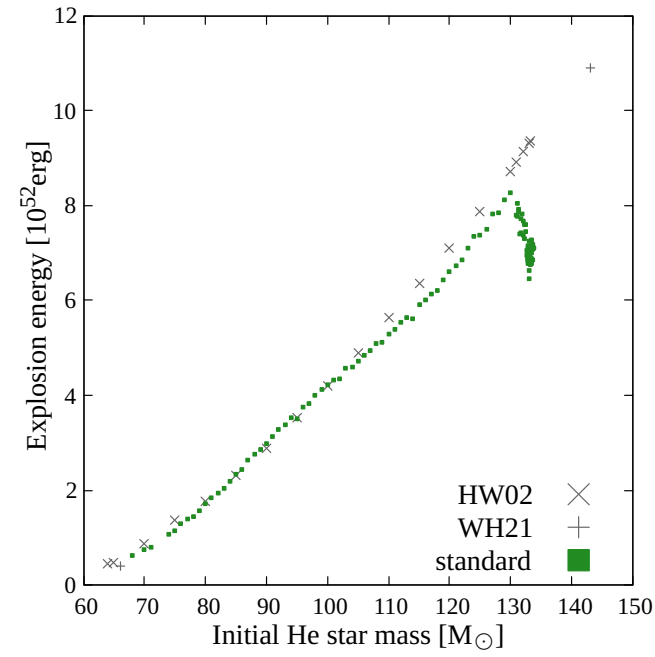


Figure C1. The consistency with Heger & Woosley (2002). The upper panel illustrates the relationship between the initial He core mass $M_{\text{init,He}}$ and the energy gained. The lower panel shows the amount of synthesized nickel. The points in both panels represent our results (green points) and the results of Heger & Woosley (2002) as HW02 and Woosley & Heger (2021) as WH21 (black points), indicating the consistency between the two studies.

Table D1. : -2σ series

initial mass (M_{\odot})	E_{expl} (10^{51} erg)	$M_{^{56}\text{Ni}}$ (M_{\odot})			
91.0	12.511	0.007	149.0	97.966	46.389
92.0	13.565	0.011	150.0	97.285	48.013
93.0	14.491	0.012	151.0	100.351	50.357
94.0	15.148	0.017	152.0	103.607	53.967
95.0	16.188	0.023	153.0	105.196	57.709
96.0	17.740	0.036	154.0	109.789	61.316
97.0	17.905	0.037	155.0	110.906	62.822
98.0	19.659	0.049	156.0	112.095	66.516
99.0	20.991	0.063	157.0	118.701	70.121
100.0	21.994	0.076	158.0	118.596	74.392
101.0	22.973	0.088	159.0	104.138	77.990
102.0	24.557	0.110	159.1	98.422	79.742
103.0	26.543	0.153	159.2	96.523	80.150
104.0	27.422	0.173	159.3	89.998	81.529
105.0	29.083	0.215	159.4	93.981	80.780
107.0	31.961	0.296	159.5	85.228	82.918
108.0	33.276	0.367	159.6	89.653	82.020
109.0	34.053	0.440	159.7	96.076	80.631
110.0	36.177	0.586	159.8	84.733	83.524
111.0	37.533	0.675	159.9	83.024	84.027
112.0	39.465	0.796	160.0	88.001	82.443
113.0	41.653	1.116	160.01	80.404	83.923
115.0	44.569	1.495	160.02	75.921	83.394
116.0	46.840	1.982	160.03	82.720	83.894
117.0	48.306	2.196	160.04	89.225	82.663
118.0	50.363	2.776	160.05	80.003	83.703
119.0	51.553	2.993	160.06	80.491	83.555
120.0	52.688	3.595	160.07	83.882	83.937
121.0	54.672	4.206	160.08	77.789	83.212
122.0	55.588	5.201	160.09	79.499	83.897
123.0	57.190	5.306	160.1	82.440	83.847
124.0	59.137	6.055	160.11	80.656	83.899
125.0	60.993	7.022	160.12	86.731	83.051
126.0	62.318	8.592	160.13	73.554	83.213
127.0	64.802	8.785	160.14	89.761	82.450
128.0	64.981	9.590	160.15	77.074	83.725
129.0	66.932	10.486	160.16	79.719	84.010
130.0	69.066	12.060	160.22	76.173	83.526
131.0	70.850	12.810	160.23	77.977	83.741
132.0	71.116	13.108	160.24	76.391	83.373
133.0	73.365	14.787	160.25	76.217	83.223
134.0	73.877	15.517	160.26	76.932	83.321
135.0	75.343	16.799	160.28	76.281	83.346
136.0	77.998	18.246	160.29	77.428	83.305
137.0	78.989	19.712	160.31	76.168	83.351
138.0	80.863	21.275	160.32	80.917	83.710
139.0	81.876	22.789	160.33	79.453	83.396
140.0	82.116	24.522	160.49	80.745	83.559
141.0	84.378	26.383	160.52	76.525	83.508
142.0	85.752	28.629			
143.0	87.495	30.692			
144.0	86.381	32.804			
145.0	90.063	34.538			
146.0	91.855	37.426			
147.0	93.466	39.716			
148.0	92.408	42.837			

Table D2. : -1σ series

initial mass (M_{\odot})	E_{expl} (10^{51} erg)	$M_{56\text{Ni}}$ (M_{\odot})			
74.0	7.170	0.015	134.0	81.016	41.012
79.0	9.399	0.024	135.0	84.518	43.547
80.0	9.714	0.026	136.0	83.404	46.625
81.0	11.255	0.040	137.0	89.058	49.512
82.0	12.849	0.055	138.0	89.519	52.361
83.0	13.463	0.076	139.0	91.803	55.047
84.0	14.358	0.086	140.0	90.872	58.948
85.0	15.355	0.101	141.0	94.032	60.384
86.0	16.787	0.121	142.0	97.760	64.096
87.0	17.663	0.150	143.0	90.491	69.568
88.0	18.500	0.168	144.0	86.285	71.598
89.0	19.957	0.182	144.01	85.633	71.902
90.0	21.099	0.213	144.02	83.705	72.380
91.0	21.642	0.260	144.03	83.856	72.417
92.0	23.826	0.335	144.04	81.452	72.970
93.0	24.461	0.402	144.05	84.354	72.144
94.0	25.751	0.412	144.06	83.028	72.477
95.0	26.964	0.523	144.07	81.435	72.296
96.0	29.625	0.726	144.08	86.281	71.683
97.0	31.303	0.869	144.09	77.677	73.805
98.0	32.449	0.981	144.1	83.377	72.524
99.0	34.073	1.206	144.11	85.262	71.912
100.0	35.767	1.701	144.12	83.812	72.445
101.0	36.711	1.744	144.13	84.712	72.191
102.0	38.357	2.178	144.14	78.819	73.635
103.0	39.083	2.522	144.15	82.745	72.670
104.0	40.338	2.652	144.16	81.625	72.870
105.0	42.147	3.292	144.17	80.822	73.170
106.0	43.150	3.984	144.18	83.814	72.396
107.0	44.906	4.233	144.19	84.197	72.469
108.0	46.386	5.052	144.2	82.223	72.834
109.0	47.471	5.451	144.21	76.990	74.119
110.0	49.144	6.656	144.22	72.112	76.712
111.0	50.694	7.341	144.23	81.681	72.950
112.0	51.694	8.260	144.24	83.911	72.346
113.0	53.226	9.224	144.25	82.540	72.780
114.0	54.030	9.820	144.26	82.702	72.858
115.0	55.743	10.569	144.27	72.887	75.738
116.0	57.082	11.669	144.28	72.693	75.593
117.0	58.430	12.263	144.29	68.573	76.750
118.0	59.269	13.408	144.3	80.757	73.438
119.0	60.361	14.256	144.31	81.063	73.303
120.0	61.457	15.980	144.32	83.499	72.629
121.0	62.898	16.536	144.33	81.958	73.052
122.0	63.296	18.233	144.34	77.951	74.020
123.0	64.621	19.771	144.35	76.581	74.347
124.0	65.938	21.064	144.36	81.908	73.198
125.0	67.707	22.702	144.37	80.035	73.670
126.0	68.622	24.241	144.38	76.972	74.246
127.0	69.045	26.123	144.39	73.778	74.717
128.0	70.868	27.851	144.4	79.943	73.615
129.0	71.624	30.474	144.41	82.622	72.953
130.0	74.146	32.511	144.42	77.958	73.928
131.0	76.305	34.457	144.43	77.921	74.111
132.0	76.731	37.393	144.44	75.815	74.624
133.0	79.800	39.175	144.45	71.716	76.499
			144.46	74.036	75.179
			144.47	76.394	74.440
			144.48	73.622	75.416
			144.49	68.581	76.881

Table D3. : Standard series

			initial mass (M_{\odot})	E_{expl} (10^{51} erg)	$M_{56\text{Ni}}$ (M_{\odot})
144.5	78.349	74.113	68.0	6.240	0.038
144.51	72.385	76.474	70.0	7.495	0.058
144.52	72.789	76.120	71.0	7.997	0.063
144.53	77.174	74.362	74.0	10.664	0.111
144.54	72.482	76.219	75.0	11.567	0.131
144.55	76.713	74.614	76.0	13.099	0.167
144.56	72.192	76.823	77.0	14.117	0.194
144.57	75.079	75.104	78.0	14.444	0.222
144.58	76.267	74.690	79.0	15.796	0.248
144.59	71.971	76.787	80.0	17.235	0.314
144.6	74.448	75.172	81.0	18.502	0.377
144.61	72.558	76.010	82.0	19.549	0.459
144.62	74.702	74.969	83.0	20.475	0.525
144.63	73.984	75.579	84.0	21.892	0.610
144.64	75.595	74.834	85.0	23.527	0.744
144.65	76.052	74.633	86.0	24.359	0.823
144.67	74.559	75.207	87.0	26.418	1.077
144.68	72.878	75.977	88.0	27.571	1.383
144.69	73.049	76.916	89.0	28.677	1.599
144.7	72.216	76.616	90.0	29.829	1.915
144.71	72.662	76.115	91.0	31.295	2.191
144.72	73.863	75.619	92.0	32.732	2.555
144.73	72.261	75.719	93.0	33.817	3.070
144.74	72.217	76.679	94.0	35.235	3.407
144.75	72.552	76.270	95.0	35.086	3.770
144.76	76.809	74.542	96.0	37.565	4.494
144.77	72.186	76.926	97.0	38.265	4.848
144.78	75.469	75.064	98.0	39.988	5.686
144.79	73.237	75.825	99.0	41.207	6.418
144.8	71.954	76.714	100.0	42.164	6.870
144.81	71.624	76.426	101.0	43.241	7.677
144.85	72.569	76.883	102.0	43.617	8.629
144.86	69.570	76.470	103.0	45.626	9.608
144.87	73.009	76.410	104.0	46.025	10.053
144.88	72.550	76.718	105.0	47.227	11.325
144.89	71.126	76.455	106.0	48.530	11.784
144.9	71.981	76.782	107.0	49.430	13.447
144.91	72.443	76.965	108.0	51.047	14.256
144.92	73.830	75.848	109.0	51.248	15.787
144.93	71.598	76.420	110.0	52.903	16.162
144.95	71.435	76.474	111.0	53.972	17.695
144.96	71.441	76.504	112.0	55.364	19.234
144.97	72.527	76.904	113.0	56.346	20.971
144.98	72.374	76.993	114.0	56.191	22.286
144.99	71.910	76.485	115.0	59.153	23.929
145.0	72.699	76.524	116.0	60.197	25.445
145.01	71.698	76.924	117.0	61.372	27.168
145.02	72.389	77.083	118.0	62.123	28.597
145.03	72.633	76.705	119.0	64.322	31.449
145.04	71.796	76.561	120.0	66.102	33.266
145.06	70.201	76.961	121.0	67.358	36.060
145.07	72.801	76.874	122.0	68.572	37.484
145.12	70.323	76.848	123.0	70.939	39.380
145.14	72.277	76.943	124.0	73.493	41.802
			125.0	73.676	44.179
			126.0	75.105	46.058

127.0	78.144	48.446	133.22	67.839	69.816
128.0	78.363	51.229	133.23	68.270	69.708
129.0	81.199	54.849	133.24	68.228	69.914
130.0	82.802	57.982	133.25	70.338	71.353
131.0	77.870	60.243	133.26	68.241	69.842
131.1	80.579	60.988	133.27	71.259	71.541
131.2	77.673	61.361	133.28	70.653	71.444
131.3	78.743	62.084	133.29	70.884	71.476
131.4	79.245	62.103	133.3	69.151	70.727
131.5	74.003	63.032	133.31	68.132	70.425
131.6	77.129	62.596	133.33	70.474	71.379
131.7	74.163	63.534	133.34	70.104	70.973
131.8	78.273	62.984	133.35	67.975	70.174
132.0	76.808	64.319	133.36	68.140	69.969
132.1	73.683	65.472	133.37	67.801	70.195
132.2	76.020	64.682	133.39	71.438	71.221
132.3	73.012	65.362	133.4	72.776	71.554
132.4	75.939	65.109	133.41	68.319	70.620
132.5	74.425	65.758	133.42	71.298	71.656
132.6	69.627	67.037	133.43	71.078	71.460
132.7	70.423	67.208	133.46	68.388	70.689
132.8	71.065	67.150	133.47	71.315	71.060
132.81	69.740	67.747	133.48	71.263	71.274
132.82	70.605	67.267	133.49	68.875	71.311
132.83	71.493	66.884	133.52	71.036	71.663
132.84	68.489	68.637	133.54	71.741	71.410
132.85	68.232	69.051	133.55	71.011	71.189
132.87	69.666	67.626	133.56	71.902	71.549
132.88	68.688	68.494	133.57	71.146	71.639
132.89	69.271	67.459	133.58	70.759	71.569
132.9	67.826	69.541	133.6	71.222	71.476
132.91	69.079	68.331	133.61	71.486	71.657
132.92	68.757	68.276	133.62	68.564	71.417
132.93	69.012	68.783	133.63	71.531	71.509
132.94	69.801	67.671	133.72	70.959	71.471
132.95	70.071	67.675			
132.96	71.615	66.949			
132.97	69.576	67.895			
132.98	66.422	69.994			
132.99	70.380	67.530			
133.0	68.945	69.203			
133.01	67.950	69.289			
133.02	68.233	69.501			
133.03	67.882	69.616			
133.04	72.622	71.147			
133.05	68.008	69.476			
133.07	67.887	70.058			
133.08	68.565	69.092			
133.09	69.631	67.935			
133.11	67.741	69.799			
133.12	68.837	69.007			
133.13	68.415	69.356			
133.14	64.707	70.551			
133.15	68.836	69.153			
133.16	68.703	69.390			
133.17	67.640	69.238			
133.18	68.021	70.517			
133.19	70.346	71.512			
133.2	70.178	71.449			
133.21	68.927	70.570			

Table D4. : $+1\sigma$ series

initial mass (M_{\odot})	E_{expl} (10^{51} erg)	$M_{^{56}\text{Ni}}$ (M_{\odot})			
63.0	4.909	0.057	121.0	71.508	49.104
64.0	5.530	0.068	122.0	72.343	51.352
65.0	6.386	0.093	123.0	73.971	54.133
66.0	7.188	0.112	124.0	71.545	57.078
67.0	7.903	0.127	124.1	68.304	58.381
68.0	8.859	0.161	124.2	71.196	57.739
69.0	9.796	0.179	124.3	70.441	59.580
70.0	10.553	0.208	124.4	67.706	59.025
71.0	11.627	0.249	124.5	71.687	58.751
74.0	14.984	0.396	124.6	68.789	60.575
75.0	16.287	0.464	124.7	66.657	58.898
76.0	17.677	0.547	124.8	71.154	59.585
77.0	18.608	0.619	124.9	69.422	60.663
78.0	19.847	0.809	125.0	67.480	61.562
79.0	20.839	0.967	125.1	64.969	61.626
80.0	22.200	1.143	125.2	66.857	61.729
81.0	23.768	1.362	125.3	67.251	62.142
82.0	24.787	1.576	125.4	66.495	62.512
83.0	25.249	1.815	125.5	65.041	63.224
84.0	27.232	2.150	125.6	63.482	64.032
85.0	27.931	2.402	125.7	64.067	63.826
86.0	29.258	2.862	125.8	63.807	64.860
87.0	30.707	3.375	125.9	63.441	64.361
88.0	31.514	3.870	126.0	64.279	64.180
89.0	33.227	4.456	126.1	63.606	65.612
90.0	33.615	4.976	126.2	62.565	66.111
91.0	34.728	5.304	126.3	64.052	65.473
92.0	36.046	6.034	126.4	63.499	66.653
93.0	37.144	6.593	126.5	65.599	67.185
94.0	37.376	7.351	126.6	68.805	68.311
95.0	38.535	8.127	126.7	67.741	67.347
96.0	39.742	8.986	126.8	70.013	68.389
97.0	40.792	9.895	126.82	69.987	68.374
98.0	41.832	10.773	126.84	69.164	68.457
99.0	41.310	11.813	126.94	71.753	68.328
100.0	43.497	12.852	127.01	70.860	68.431
101.0	45.750	13.571			
102.0	45.761	14.465			
103.0	47.208	15.755			
104.0	48.032	17.312			
105.0	49.331	18.219			
106.0	51.329	20.039			
107.0	51.282	20.848			
108.0	52.897	22.548			
109.0	53.983	23.793			
110.0	55.974	25.831			
111.0	57.185	27.934			
112.0	57.329	29.424			
113.0	58.524	30.888			
114.0	59.956	32.975			
115.0	62.742	34.845			
116.0	64.067	37.750			
117.0	65.201	39.029			
118.0	67.094	41.626			
119.0	68.388	43.900			
120.0	69.560	46.244			

Table D5. : $+2\sigma$ series

initial mass (M_{\odot})	E_{expl} (10^{51} erg)	$M_{56\text{Ni}}$ (M_{\odot})			
62.0	5.168	0.094	120.0	70.208	53.058
63.0	5.601	0.107	121.0	70.360	55.208
64.0	6.771	0.146	122.0	64.158	58.613
65.0	7.318	0.160	122.1	68.107	58.602
66.0	8.282	0.200	122.2	66.929	59.605
67.0	9.115	0.228	122.3	65.394	60.342
68.0	10.090	0.278	122.4	64.910	60.743
69.0	10.873	0.314	122.5	64.897	60.986
70.0	11.924	0.372	122.6	63.419	61.801
71.0	13.259	0.420	122.7	65.228	60.991
74.0	16.293	0.671	122.8	64.114	61.564
75.0	17.978	0.812	122.9	65.710	60.871
76.0	19.010	0.925	123.0	61.331	62.886
77.0	20.149	1.081	123.1	63.446	62.239
78.0	21.031	1.256	123.2	62.255	62.935
79.0	22.249	1.544	123.3	61.668	63.326
80.0	23.523	1.742	123.4	60.687	65.230
81.0	24.837	1.982	123.5	61.747	64.110
82.0	25.629	2.409	123.51	61.447	64.023
83.0	26.943	2.804	123.52	62.790	65.918
84.0	28.474	3.173	123.53	61.549	64.787
85.0	29.029	3.563	123.54	61.548	65.766
86.0	30.532	4.180	123.55	60.147	65.254
87.0	31.487	4.634	123.56	62.826	65.865
88.0	32.323	5.263	123.57	67.677	67.828
89.0	33.357	5.956	123.58	63.448	66.479
90.0	34.177	6.609	123.59	61.153	65.534
91.0	35.029	7.210	123.6	61.302	64.261
92.0	35.650	7.794	123.61	65.898	66.804
93.0	37.320	8.841	123.62	62.101	65.720
94.0	38.419	9.638	123.63	61.594	65.054
95.0	39.351	10.456	123.64	61.831	64.129
96.0	40.946	11.014	123.65	67.152	67.388
97.0	41.039	12.424	123.66	66.822	66.942
98.0	42.794	13.369	123.67	67.618	67.739
99.0	43.395	14.086	123.68	67.422	67.129
100.0	44.096	15.392	123.69	62.012	65.757
101.0	45.714	16.049	123.7	61.935	64.768
102.0	46.174	17.791	123.71	65.099	66.553
103.0	47.341	19.134	123.72	67.810	67.841
104.0	48.465	20.343	123.73	67.462	67.800
105.0	50.321	21.532	123.74	67.587	67.395
106.0	51.305	23.892	123.75	67.661	67.750
107.0	52.732	24.599	123.76	67.374	67.832
108.0	53.743	27.496	123.77	65.010	66.515
109.0	54.998	28.276	123.78	66.153	66.885
110.0	55.483	30.123	123.79	66.355	66.812
111.0	57.199	32.132	123.8	66.547	67.720
112.0	58.933	33.544	123.81	65.491	66.499
113.0	59.932	35.889	123.82	65.223	66.380
114.0	61.076	38.316	123.83	68.037	67.732
115.0	63.123	40.034	123.84	63.912	66.333
116.0	63.940	42.771	123.86	68.657	67.671
117.0	66.161	44.690	123.87	68.888	67.649
118.0	68.065	47.874	123.89	61.794	65.516
119.0	68.997	50.647	123.9	66.043	66.694
			123.92	66.373	67.842
			123.93	66.742	67.330
			123.94	66.909	67.110
			123.96	69.205	67.526

123.97	67.497	67.685
123.98	68.122	67.855
123.99	68.304	67.889
124.01	67.928	67.724
124.02	67.844	67.797
124.04	66.779	67.160
124.06	68.770	67.596
124.08	67.790	67.015
124.09	67.828	67.657
124.1	66.976	67.763
124.15	70.237	67.604

This paper has been typeset from a $\text{\TeX}/\text{\LaTeX}$ file prepared by the author.